PAPER

Check for updates

A MoS₂ quantum dot functionalized TiO₂ nanotube array for selective detection of xylene at low temperature

Radha Bhardwaj and Arnab Hazra [iD] *

Xylene is among the most complex volatile organic compounds (VOCs) and is significant in many applications. Xylene as an efficient breath marker of lung cancer raises the concern of discrimination between compounds having chemically similar nature like benzene, toluene, *etc.* For highly stable and selective detection of xylene, in this study, we report a 0D–1D nanocomposite, *i.e.* a MoS₂ quantum dot (QD) functionalized TiO₂ nanotube array. The nanocomposite synthesis involves a hydrothermal reaction between MoS₂ QDs and the 1D TiO₂ nanotube array which is synthesized by anodic oxidation of titanium foil. The Au/MoS₂–TiO₂ nanotube/Ti structured sandwich type sensor exhibited selective xylene detection with a high response magnitude of 188% (50 ppm xylene) which is many times higher than those of the pure MoS₂ QD and TiO₂ nanotube sensors at a relatively low operating temperature, *i.e.* 75 °C. It also displayed a fast response time (35 s) and maximum recoverability, with a lower detection limit (LOD) of 33 ppb. Notably, the highest selectivity of detection towards xylene over benzene and toluene makes the sensor potential for environmental and breath VOC monitoring. Additionally, the long-term stability of the sensor was apparent from the stable sensing behavior even after 1 month.

1 Introduction

BTX aromatic hydrocarbons are the most complex and critical volatile organic compounds emitted from printing, paint, rubber, polymer, leather, and pharmaceutical industries which cause severe indoor air pollution and health damage.[1] Long-term exposure to such toxic VOCs damages the nervous system, depending on the exposure, concentration, and time. The US National Institute for Occupational Safety recommends a permitted exposure limit (PEL) for xylene vapor of 100 ppm for an 8 h time-weighted average (TWA).[2,3] Apart from this, xylene is an efficient breath marker for lung cancer, and in the exhaled breath of a patient, xylene concentration gets increased from 20 ppb to 100 ppb.[4,5] The selective detection of xylene breath markers among the complex chemically similar VOCs is also a significant concern.[6,7]

Various perovskites, metal oxides and their nanocomposite materials such as ZnCo₂O₄ microspheres,[8] Co₃O₄–In₂O₃ hetero-structure,[9] Zn-doped α-Fe₂O₃ nanoparticles,[10] and AgCu/TiO₂ nanoparticles[11] have been employed for the selective detection of xylene vapor, but their high-temperature working (>150 °C)

causes a significant concern over the complexity and long-term stability of the sensor. Among all metal oxides, TiO₂ is a promising gas-sensing element due to its wide bandgap (≈ 3.2 eV), high catalytic activity, oxygen adsorption characteristics, non-toxicity, and environmental friendliness.[8–14] The anatase phase of TiO₂ has more catalytic activity and the optimum bandgap promotes easy electron transfer from TiO₂ to adsorbed VOC molecules, thus proving better suitability in the sensing field.[15] One more advantageous aspect of TiO₂ is that it can be tailored into different nano-dimensional morphologies like $\sim$0D (nanoparticles),[16] 1D (nanotubes),[17] 2D (thin films),[12] *etc.* Among them, 1D TiO₂ possesses fast electron transfer, uniformity, higher morphological stability, and a higher specific surface area, leading to low operating temperature of the material.[17,18] Bindra *et al.* explored the selective detection of organic vapors using a TiO₂ nanotube-based gas sensor.[17] Doped nanotubes presented a high response magnitude of 60% under exposure to 100 ppm of ethanol at a lower operating temperature of 50 °C.[19] However, lower selectivity and poor sensing response remain challenges for the pristine 1D TiO₂ nanotube sensors.[17,20]

In recent years, 2D transition metal dichalcogenides (TMDs) have become more acceptable and demanding nanomaterials and have been efficiently employed in various applications such as gas sensing,[21,22] hydrogen evolution,[23] water splitting,[24] photodetectors[25] and so on. TMDs are represented with a

Dept. of Electrical and Electronics Engineering, Birla Institute of Technology and Science (BITS)-Pilani, Vidya Vihar, Rajasthan 333031, India.
E-mail: arnabhazra2013@gmail.com, arnab.hazra@pilani.bits-pilani.ac.in;
Tel: +91-1596-255724

common formula of MX_2, where M is a transition metal (Mo, Sn, W, Ni, *etc.*) and X denotes chalcogens (S, Se, Te). The advancement of TMDs in various applications is attributed to their intriguing electronic, optical, chemical, physical, and magnetic properties.[26] The presence of electronic bandgaps in TMDCs makes them suitable for semiconducting gas-sensing materials and till now MoS_2,[21,22,27,28] WS_2,[29–31] $MoSe_2$,[32] and WSe_2[33] have been employed for efficient gas sensing applications. Among them, MoS_2 with abundant reactive sites possesses high sensitivity and easy surface functionalization possibilities for VOC sensing applications.[21,22,27,28,34–36] Kim *et al.* synthesized a mercaptoundecanoic acid (thiolated ligand)-conjugated MoS_2 sensor to achieve high sensitivity towards low ppm VOCs.[34] TMDCs are the most famous for the selective detection of VOCs but unfortunately suffer from slow response/recovery, low chemical stability, and low response behavior, which require modification of their sensing properties.[37]

Considering the individual advantages of metal oxides and TMDs, potential composites can be prepared for high-performance gas/VOC sensing applications. The unique morphology of composite materials also plays a significant role in the modification of material properties, significantly improving the sensing characteristics of the material. In this regard, the functionalization of sensing materials with nanoparticles (Au,[30,38] Pt[27]) and quantum dots (WS_2,[31] MoS_2[28]) results in chemical and electrical sensitization in the material. The electrical sensitization leads to the formation of discrete Schottky junctions due to their work function differences.[38] More specifically, quantum dots are the smallest nanomaterials whose size varies from 1 to 10 nm showing immense potential in device applications.[28] Singh *et al.* synthesized highly sensitive and stable sensors based on the thin film of a MoS_2/TiO_2 composite. The device has shown a 100% response for ethanol with a superior signal-to-noise ratio at 300 °C.[12] However, the high operating temperature is also a significant concern for thin film-based sensors.

Herein, for the first time, we prepared a 0D–1D-based MoS_2/TiO_2 composite to overcome the issue of poor selectivity and higher operating temperature in VOC sensing. A TiO_2 nanotube array was synthesized by anodic oxidation and functionalized with MoS_2 quantum dots to achieve superior xylene selective sensing compared to chemically similar compounds like benzene and toluene. MoS_2 functionalized TO_2 nanotubes were implemented in a metal–insulator–metal (MIM) type sensor structure and operated at 75 °C to achieve excellent xylene selectivity. The sensor showed good response behavior with outstanding long-term and signal stability.

2 Materials and methods

2.1 Synthesis of the TiO_2 nanotube array

The TiO_2 nanotube array was synthesized by a simple electrochemical anodization method. A 2 cm × 2 cm Ti foil (0.25 mm thickness, purity > 99.9%) was cleaned thoroughly by sonication for 10 minutes in each of the following solvents: acetone, ethanol, and deionized water. After that, 2 M of HF (48% purity, Sigma-Aldrich) etching was performed to provide suitable roughness for better growth of nanotubes. Anodization was done in two steps: the first step was carried out for 90 min at 60 V using a power supply in a two-electrode system with a graphite counter electrode. Consecutively, another anodization reaction was carried out for 1 min at the same 60 V constant voltage. Both anodization reactions took place in different electrolyte solutions containing predetermined ratios of ethylene glycol, water, and ammonium fluoride. The detailed procedure for anodic oxidation has already been described in our earlier reports.[17,39] This two-step anodization helps to remove the initial oxide layer from the top of the nanotube array and leads to the open-pore structure. The TiO_2 nanotube array on a Ti substrate (or foil) was annealed in air at 450 °C for 4 h to make it mechanically robust and improve the amorphous TiO_2 to anatase ratio.

2.2 Preparation of MoS_2 quantum dots

MoS_2 was purchased from Sigma-Aldrich and further proceeded without any purification. 2 mL of MoS_2 suspension was dispersed into 100 mL of deionized water and sonicated for 1 hour. The resulting sonicated suspension was then centrifuged at 4500 rpm for 10 min. The resulting supernatant was collected and then used further for composite formation.

2.3 Synthesis of the MoS_2/TiO_2 nanotube heterostructure

MoS_2 quantum dot (QD) coated TiO_2 nanotubes were synthesized with one-step hydrothermal treatment. The TiO_2 nanotube/Ti samples were placed inside a Teflon-lined autoclave containing 2.8 mg MoS_2 in 100 mL of deionized water and maintained at 180 °C for 18 h. The resulting sample was washed with absolute ethanol and deionized water to remove excess MoS_2 and then dried in nitrogen. The MoS_2/TiO_2 heterostructure nanotube array was thermally treated at 150 °C for 3 h in the air to provide thermal stability to the heterostructure.

2.4 Characterizations

An Apreo LoVac field emission scanning electron microscope (FESEM) operating at an accelerating voltage of 5 kV was used for scanning electron microscopy (SEM). A Tecnai G2 20 S-TWIN [FEI] system was used for the transmission electron microscopy (TEM) measurements, as well as the high-resolution transmission electron microscopy (HRTEM) measurements (acceleration voltage: 200 kV). A Bruker AXS D2 PHASER XRD was used to collect the X-ray diffraction (XRD) results with CuKα radiation (1.5418 Å) in the range of 10–70°. X-ray photoelectron spectroscopy (XPS) data were measured using a Thermo Fisher Scientific K-Alpha setup (base pressure of 10^{-9} mbar) with an Al Kα micro-focused monochromator (hv = 5–1500 eV) for excitation. The Raman spectra were collected on a LabRAM HR Evolution Omega Scope with a 532 nm laser. The operating voltage was set to 200 kV.

2.5 Device fabrication and sensor setup

The 1D TiO_2 nanotubes and MoS_2/TiO_2 heterostructure nanotube array were well suited for the metal–insulator-metal (MIM) type device structure. The Ti substrate with vertically aligned

nanotubes was considered as the bottom metal electrode. And 150 nm thick Au electrodes were deposited on the top surface of the nanotubes by the electron beam evaporation technique at a 10^6 mbar vacuum pressure. An Al metal mask with a 1 mm × 1 mm opening was used to deposit the top electrode. The details of TiO_2 nanotube-based MIM structure sensors are provided in our earlier reports.[17,19]

The gas measurement setup includes a customized sealed gas chamber with an inlet and an outlet for gas flow. The chamber is connected with a customized injection system and mass flow controllers (MFCs, Alicat Scientific, Inc.) for target VOC injection and carrier gas (dry air/nitrogen (N_2)/argon (Ar)) flow, respectively. VOCs were injected using microsyringes (Hamiltonian) ranging in concentration from 1 μL to 500 μL following their ppm value. The ppm value for a particular VOC has been discussed in our previously reported studies.[38,40] The total flow inside the chamber was maintained constant at 600 sccm for each VOC to abolish the effect of change in pressure due to the different flow rates on sensor response. The electrical signals of the device were recorded using a B2900 source/measure unit (SMU, Keysight Technologies) which was connected to the device by electrical feed-throughs. The sensor response was recorded at 1 V bias potential. The sensing magnitude (SM) was calculated using the following formula: $(\Delta R/R_a) \times 100$, where ΔR is the change in baseline resistance from air to VOC or VOC to air and R_a is the baseline resistance in the air.

3 Results and discussion

3.1 Materials characterizations

The surface morphology of the prepared TiO_2 nanotube array before and after the hydrothermal treatment with MoS_2 QDs was analyzed using the FESEM technique. The nanotube morphology was intact after MoS_2 functionalization, the pore diameter was decreased significantly and the average pore diameter was measured as 95 nm for pristine TNTs and 70 nm for MoS_2/TNTs as shown in Fig. 1(a and c). MoS_2 QDs were aggregated, and small clusters of different dimensions were decorated on the TiO_2 nanotubes. The distribution of pure MoS_2 quantum dots can be visualized in Fig. 1(b). It was anticipated that the surface roughness of the TNTs would be enhanced due to the decoration of individual and aggregated MoS_2 (Fig. 1(c)). However, the decoration of MoS_2 on the sidewall of the TiO_2 nanotubes is not meaningfully evident from the FESEM image (Fig. 1(c)). Consequently, a detailed TEM analysis was performed to determine the decoration of small and individual MoS_2 QDs on the top of the TiO_2 nanotube surface. The uniform decoration of MoS_2 QDs was observed on the top and side walls of the nanotubes (Fig. 1(d and e)). The TEM analysis ensured that the MoS_2 QDs had relatively small dimensions (5–10 nm) compared to the average cluster size (Fig. 1(d)). The side wall of the nanotube is fully decorated with the MoS_2 QDs in Fig. 1(e). The high-resolution TEM (HRTEM) image in Fig. 1(f) shows the MoS_2/TNTs side wall interface where the inter-planar distance of 0.375 nm corresponds to the (101) crystal plane of anatase[17,19] and 0.75 nm corresponds to the (002) crystal plane of MoS_2 showing less crystalline and non-homogenous lattice arrangement of the resulting QDs which is in good agreement with previously reported works.[41,42]

To understand the crystalline nature of MoS_2, TiO_2, and MoS_2/TiO_2 NT composites, X-ray diffraction spectra were recorded and are presented in Fig. 2(a). The sharpest and most intense peak at 24.7° confirmed the significant contribution of anatase (101) crystallinity in TiO_2 nanotubes.[17,19] However, Fig. 2(a) illustrates a few small peaks of rutile crystallinity following the hydrothermal and heat treatment in both samples (Fig. 2(a)). A small rutile (110) peak was observed near 28.8°.[19,39] The other low-intensity peaks at 38.7° and 68.2° in
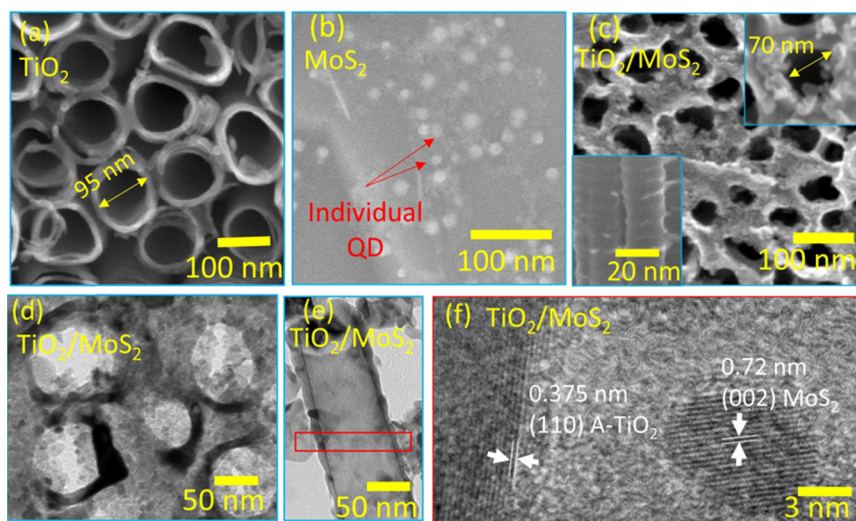

Fig. 1 SEM micrographs of (a) pure TiO_2 nanotube arrays, (b) MoS_2 quantum dots, and (c) a MoS_2/TiO_2 composite; (d) and (e) TEM image of the MoS_2/TiO_2 composite and (f) HRTEM image showing the coexistence of TiO_2 and MoS_2.
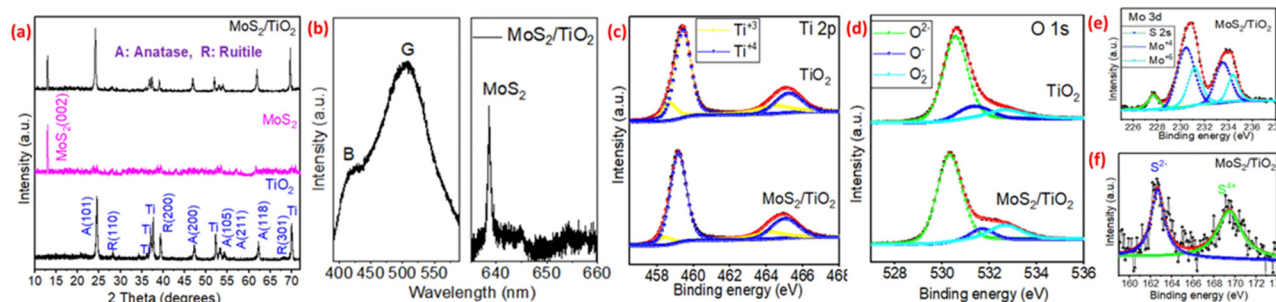
Fig. 2 (a) XRD spectra of TiO_2 nanotubes, MoS_2 QDs, and the MoS_2/TiO_2 composite. (b) PL spectra of the MoS_2/TiO_2 composite. High-resolution XPS spectra and peak positions of (c) Ti 2p, (d) O 1s, (e) Mo 3d, and (f) S 2s spectra of TiO_2 nanotubes and the MoS_2/TiO_2 nanotube composite.

pure TiO_2 nanotubes correspond to rutile (200) and (301) crystallinity, respectively. A few low-intensity anatase peaks of (200), (105), (211), and (118) crystallinity were observed at $46°$, $53.5°$, $54.61°$, and $62.2°$, respectively. A few peaks of metallic Ti from the Ti-substrate were also observed in both samples (Fig. 2(a)). The XRD spectra of pure MoS_2 confirmed the (002) orientation at $14.2°$ ensuring the existence of pure MoS_2.[42] The coexistence of both materials was confirmed by the XRD spectra of the MoS_2/TiO_2 NT composite (Fig. 2(a)).

The PL spectra in Fig. 2(b) show two main peaks centred at 412 nm and ~ 502 nm which correspond to the band to band emission and defect assisted recombination due to the presence of huge oxygen vacancies in TiO_2, respectively.[17,39] One peak centred at ~ 639 nm is related to the MoS_2 in the TiO_2/MoS_2 composite.[43] The PL results coincide with the XPS results in Fig. 2(c–e) and the presence of MoS_2 QDs on the TiO_2 nanotube surface is traced more efficiently by X-ray photoelectron spectroscopy.

X-ray photoelectron spectroscopy (XPS) was carried out on pure TiO_2 and MoS_2/TiO_2 composite samples to examine their chemical states and surface compositions. Ti 2p peaks were found at 459.3 and 465.2 eV with a spin–orbit doublet separated by 5.9 eV, which infers two oxidation states into the resulting material (Fig. 2(c)). The peaks were deconvoluted based on oxidation into the resulting samples and observed at 458.5 eV, 459.7 eV, 464.1 eV, and 465.4 eV corresponding to Ti^{3+} $2p_{3/2}$, Ti^{4+} $2p_{3/2}$, Ti^{3+} $2p_{1/2}$ and Ti^{4+} $2p_{1/2}$, respectively. The intensity and area of Ti^{3+} peaks are significantly lower than those of Ti^{4+} peaks in the MoS_2/TiO_2 composite compared to the pure TNTs confirming the improved surface oxygen in the TiO_2 nanotube array after MOS_2 functionalization (Fig. 2(c)). The O 1s spectra in Fig. 2(d) showed three peaks at 530.6, 531.9, and 533.5 eV corresponding to O^{2-} (lattice oxygen), O^{-} (oxygen vacancies), and O^{-}_2 (chemisorbed oxygen), respectively.[39] The higher area of the chemisorbed oxygen peak compared to the lattice oxygen and oxygen vacancy in the MoS_2/TiO_2 composite could arise due to highly chemically sensitized MoS_2 QDs which helps in the more gaseous analyte interaction during the sensing experiments.[44] The Mo 3d signal comes from the peaks around 229.2, 231.1, 233.2, and 235.1 eV matching with the Mo^{4+} $3d_{5/2}$, Mo^{4+} $3d_{3/2}$, Mo^{6+} $3d_{5/2}$ and Mo^{5+} $3d_{3/2}$ of MoS_2, respectively (Fig. 2(e)).[12,44] The adsorption of surface oxygen functional groups or partial oxidation on the surface of MoS_2 QDs generates Mo^{6+} states which help in the gaseous interaction.[12,45] It should be pointed out that both Mo and S peaks were observed in the Mo 3d spectrum of the MoS_2/TiO_2 composite, suggesting its origin from the MoS_2 component.[45] The two characteristic peaks (S^{2-} $2p_{3/2}$ and S^{2-} $2p_{1/2}$) of S 2s spectra merged into one and observed at 162.9 eV originating from the edge-located S_2^{2-} which are recognized as the active sites of MoS_2 (Fig. 2(f)).[45] At a higher binding energy of 169.7 eV, a significant peak was observed for S^{4+}, further confirming the +6 oxidation state of Mo. The highly oxidized surface of MoS_2 contains many reactive sites.[12] Additionally, MoS_2/TiO_2 heterostructure formation will lead to more defect sites, and as the defects are increased, it induces the change of the local electron distribution of Mo and S in the heterojunction which provides electronic sensitization in the resulting composite sensor.[45]

3.2 Sensor study

To optimize the best-suited working temperature, the VOC sensing behavior of the prepared sensors was analyzed at temperatures in the range of 45–90 °C. The baseline resistance was decreased abruptly while increasing the temperature from 45 °C to 90 °C. The literature also confirmed the stable sensing performance of MoS_2 at a relatively low temperature (Fig. 3(a)).[37,38] The response of MoS_2, TiO_2, and MoS_2/TiO_2 sensors was evaluated with 50 ppm of xylene in air at different temperatures as shown in Fig. 3(b). The response curve exhibited a dip tendency beyond 75 °C displaying a volcano-shaped curve (Fig. 3(b)). For MoS_2/TiO_2 nanotube sensors (Fig. 3(b)), the response magnitude increased linearly from 45 °C to 90 °C and showed a sharp increment in response magnitude at 75 °C. Moreover, the MoS_2/TiO_2 sensor showed a pretty high response, i.e., $\sim 188\%$, which is many times higher than those of the pure MoS_2 and TiO_2 sensors at a 75 °C temperature. Fig. 3(c) shows the response and response/recovery time characteristics of sensors at 75 °C optimized temperature in the air atmosphere.

The response time and recovery time for the MoS_2/TiO_2 sensor are 35 s and 335 s with an excellent response (188%) to 50 ppm xylene, which is much faster than the pure TiO_2 and MoS_2 sensors at 75 °C (Fig. 3(c)). The quick response and recovery are mainly attributed to the fast electron transfer kinetics of pure MoS_2 and TiO_2 nanotubes combined
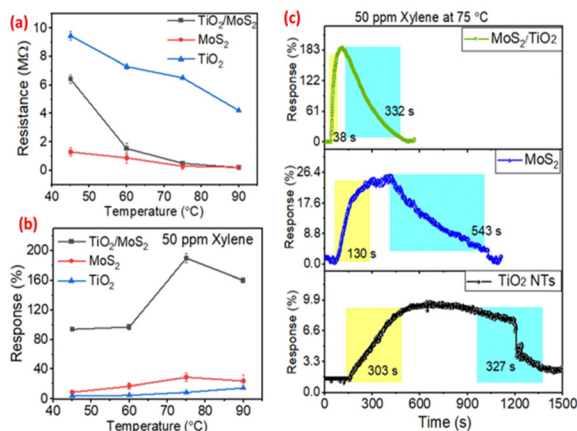
Fig. 3 (a) Baseline resistance change *vs.* temperature, (d) corresponding response magnitude ($\Delta R/R_a$ in %) *vs.* temperature for all three sensors, and (c) response characteristics of all three sensors at optimized 75 °C temperature.

throughout the composite.[17,38] It should be noted that previously reported pure TiO$_2$ sensors require a relatively high operating temperature for VOC adsorption or desorption.[19] Therefore, the MoS$_2$ modification on the TiO$_2$ nanotube significantly reduces the operating temperature of the sensors. The results were better than those obtained previously with MoS$_2$/TiO$_2$ thin film-based composites at a 240 °C operating temperature.[12] The 1D nature of TiO$_2$ nanotubes also played a significant role by offering both inner and outer surfaces for adsorption–desorption which increases the reactivity of the sensor compared to the thin film of TiO$_2$.[12,17]

To further evaluate the sensing response, the MoS$_2$ QD functionalized TiO$_2$ nanotube sensor was tested with different concentrations of xylene ranging from 150 ppm to 0.5 ppm at an optimum temperature of 75 °C. From the results, the response characteristics show a rapid change of resistance upon exposure to variable concentrations of xylene, and beyond 100 ppm, a relatively slow variation with increasing xylene concentrations is observed (Fig. 4(a)). Upon exposure to VOCs, the sensor showed increased resistance behavior, indicating the p-type response characteristics (Fig. 4(a)). The p-type behavior could be due to the p-type gas-sensing factors of MoS$_2$ QDs, which have been attributed to completely depleted MoS$_2$ QDs in environmental oxygen.[37] The high response magnitude of 69%, even at a lower concentration of 500 ppb of xylene, might arise due to the availability of the effective surface area establishing an intimate contact between two different heterostructured materials.[45] The MoS$_2$/TiO$_2$ sensor exhibited a nearly linear response to xylene ($R^2 > 0.971$) (Fig. 4(b)), suggesting the most excellent linearity and reproducibility favorable to a more extensive detection range and a lower detection limit (LOD) of 33 ppb. The selectivity of the MoS$_2$/TiO$_2$ sensor was also measured by comparing it with various VOCs (*e.g.*, acetone, methanol, ethanol, 2-propanol, formaldehyde, *n*-pentane, benzene, toluene, and xylene), as shown in Fig. 4(c). The results indicated that the MoS$_2$/TiO$_2$ sensor had a focused selectivity towards xylene. The sensor showed excellent selectivity towards

xylene (aromatic) compared to chemically different VOCs like methanol (alcohol), acetone (ketone), *n*-pentane (hydrocarbons), and formaldehyde (aldehyde) (Fig. 4(c)). Additionally, interfering aromatic VOCs with identical chemical properties like benzene and toluene showed negligible response compared to xylene. Benzene with maximum resonance behavior requires a huge dissociation energy for the interaction, whereas toluene with less electron-donating capacity than xylene makes the composite more favorable for xylene selective sensing.[46] The repeatability and long-term stability of the composite sensor are crucial parameters for a practical environment. The sensor showed remarkable consistency in a 30-day study with a one-day interval (Fig. 4(d)). The repeatable nature of the sensor was tested for 6 consecutive cycles and a variation of less than ±4% in relative response magnitude was recorded (Fig. 4(e)).

The sensing characteristics of a sensor in the presence of humidity determine the environmental stability of a sensor. Therefore, the sensor was tested in different humidity levels, ranging from RH 20% to 80% that ultimately led to understand the environmental stability of the sensor (Fig. 5). The measurements include changes in the transient characteristics, baseline resistance, response/recovery time, and response magnitude of the sensor. The baseline resistance was decreased abruptly with rising RH levels due to the removal of adsorbed oxygen species on the sensing surface (Fig. 5(f)). The response magnitude also decreased significantly when the RH changed from 20% to 80% in the composite sensor. The response/recovery time also varies with the change of the humidity level (Fig. 5(a–e)). In the presence of humidity, the water poisoning effect dominates the sensor, and the adsorption of VOC molecules becomes competitive with the water molecule, resulting in a decreased response magnitude.[12]

Moreover, the VOC sensing characteristics, stability, and excellent xylene selective sensing performance of the MoS$_2$/TiO$_2$ sensor were mainly attributed to the following: (i) controlled 1D morphology with defective nature (oxygen vacancy) that was eventually responsible for sufficiently high active sites, (ii) formation of discrete p–n heterojunctions, and (iii) unique structural and electronic properties contributing to higher recoverability and durability of the sensor.[45] In detail, the grown n-type semiconducting 1D TiO$_2$ nanotubes have a huge number of gas adsorption sites and adsorbed oxygen species confirmed by the XPS spectra (Fig. 2(c and e)), which make them more sensitive towards gaseous analytes.[17,18] On the other hand, MoS$_2$ QDs showed p-type gas sensing characteristics due to their complete depletion in environmental oxygen owing to the large specific surface area. Additionally, the work function of TiO$_2$ nanotubes and MoS$_2$ is 5.1 and 4.47 eV, respectively, and the optical band gap of TiO$_2$ ($\sim$3.2 eV)[16,17] is higher than that of MoS$_2$ ($\sim$1.8 eV).[12] Since the work function of TiO$_2$ is higher than that of MoS$_2$, the electrons will be transferred from the MoS$_2$ conduction band to TiO$_2$ creating a wider accumulation region at the interface of the MoS$_2$/TiO$_2$-based p–n heterostructure. Under ambient conditions, the heterostructure adsorbs the ambient oxygen to form O^{2-} ions
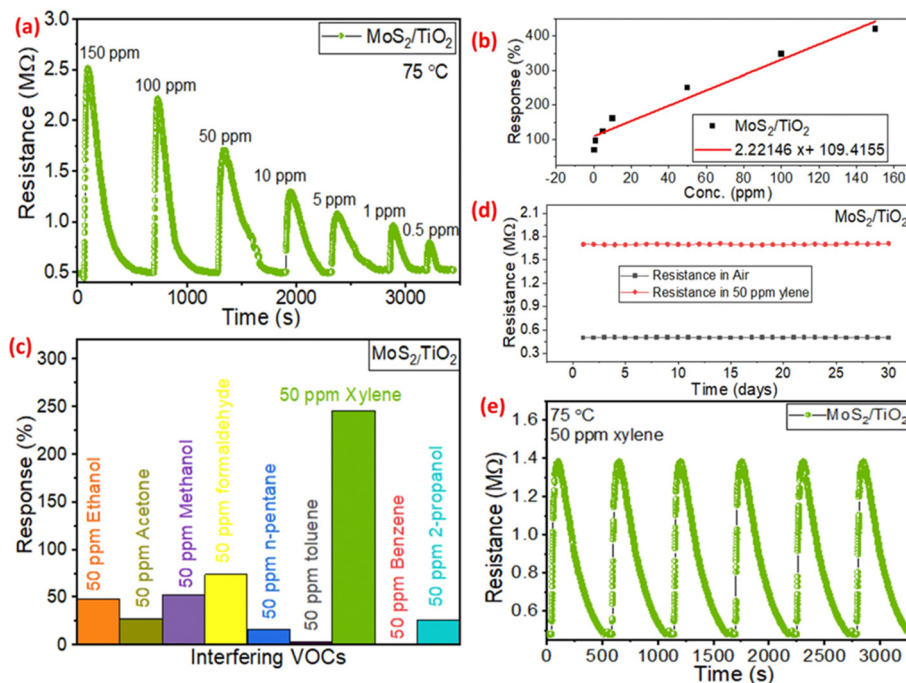
Fig. 4 (a) MoS$_2$/TiO$_2$ nanotube sensor resistance change for different xylene concentrations (in ppm). (b) Corresponding absolute response magnitude *vs.* xylene concentration (in ppm). (c) Selectivity study of xylene over other interfering VOCs, (d) long-term stability study of the sensor for 30 days with an interval of 1 day, and (e) repeatability test for six continuous cycles at a 50 ppm concentration. All measurements were performed at an optimized temperature of 75 °C.
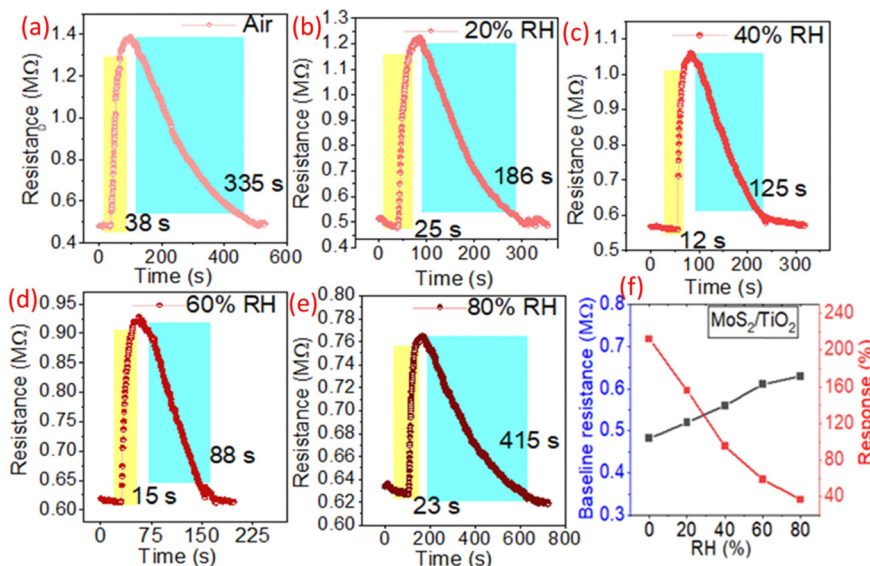

Fig. 5 (a–e) MoS$_2$/TiO$_2$ sensor resistance variation with different relative humidity levels (air, 20–80% RH) at a fixed xylene concentration of 50 ppm at 75 °C and (f) change in the baseline resistance and response magnitude (%) of the MoS$_2$/TiO$_2$ sensor at different humidity levels.

which readily combine with xylene vapor and release electrons back to the MoS$_2$ from TiO$_2$ leading to a decrease in the accumulation region. In other words, the reduced VOC interaction on the composite increased the resistance significantly as compared to TiO$_2$ or MoS$_2$, resulting in an enhanced sensing response. Furthermore, the chemical sensitization effect of

MoS$_2$ quantum dots also facilitates faster adsorption and dissociation of the xylene vapor to facilitate low-temperature sensing. Moreover, higher selectivity towards xylene is ascribed to the highly oxidizing functional groups and superficial electrons in MoS$_2$ and the catalytic action of the Mo-based material which benefit the adsorption of aromatic molecules like xylene

with high sensitivity.[45–47] Additionally, the lower sensitivity of the nanocomposite towards chemically similar aromatic VOCs like benzene and toluene could be attributed to their maximum resonance behavior, and less electron-donating capacity compared to xylene vapor.[46]

4 Conclusions

In conclusion, we have established a one-step hydrothermal strategy to integrate two different materials based on a MoS_2/TiO_2 heterostructured nanocomposite. In this construction, 1D TiO_2 nanotube arrays were first synthesized by an electrochemical anodization route. Simultaneously, MoS_2 quantum dots (QDs) on the TiO_2 nanotube array formed a continuous heterojunction network after the hydrothermal reaction. The excess specific surface area and many heterointerfaces endow MoS_2/TiO_2 with many VOC interactive sites. The tight heterointerface contacts accelerated the electron mobility in 1D TiO_2 nanotubes. Owing to the improved surface and electronic properties, the MoS_2/TiO_2 composite showed extraordinary xylene selective characteristics with a high response magnitude of 188% for 50 ppm at a 75 °C operating temperature. Most importantly, high xylene selectivity was observed in the cross interference of chemically similar VOCs like benzene and toluene. The selective xylene sensing might be due to oxidizing functional groups, superficial electrons in MoS_2, and the catalytic action of the Mo-based material. This research is focused not only on the highly sensitive, selective, and long-term stable detection of xylene but also on reducing the operating temperature of metal oxide-based sensors.

Author contributions

Radha Bhardwaj: experiments and writing. Arnab Hazra: research planning, supervision, and revision.

Data availability

The datasets used and analysed during the current study are available from the corresponding author upon reasonable request.

Conflicts of interest

There are no conflicts to declare.

Acknowledgements

References

1 S. Yang, G. Lei, H. Xu, Z. Lan, Z. Wang and H. Gu, *Nanomaterials*, 2021, **11**, 1–26.

2 H. Liu, G. Meng, Z. Deng, K. Nagashima, S. Wang, T. Dai, L. Li, T. Yanagida and X. Fang, *ACS Sens.*, 2021, **6**, 4167–4175.

3 C. Feng, C. Wang, H. Zhang, X. Li, C. Wang, P. Cheng, J. Ma, P. Sun, Y. Gao, H. Zhang, Y. Sun, J. Zheng and G. Lu, *Sens. Actuators, B*, 2015, **221**, 1475–1482.

4 R. Guo, X. Shang, C. Shao, X. Wang, X. Yan, Q. Yang and X. Lai, *Sens. Actuators, B*, 2022, **365**, 131964.

5 G. Gregis, J. B. Sanchez, I. Bezverkhyy, W. Guy, F. Berger, V. Fierro, J. P. Bellat and A. Celzard, *Sens. Actuators, B*, 2018, **255**, 391–400.

6 H. Yamagiwa, S. Sato, T. Fukawa, T. Ikehara, R. Maeda, T. Mihara and M. Kimura, *Sci. Rep.*, 2014, **4**, 1–6.

7 S. Zhao, J. Lei, D. Huo, C. Hou, X. Luo, H. Wu, H. Fa and M. Yang, *Sens. Actuators, B*, 2018, **256**, 543–552.

8 S. Wang, R. Jiang, S. Yan, M. Du, L. Zhang, Y. Feng, C. Hu and J. Cao, *Sens. Actuators, B*, 2023, **396**, 134576.

9 R. Makole, Z. P. Tshabalala, M. Jozela, F. R. Cummings, H. C. Swart and D. E. Motaung, *Inorg. Chem. Commun.*, 2023, **158**, 111652.

10 M. Du, L. Zhang, R. Jiang, C. Hu, Y. Feng, S. Wang and J. Cao, *Colloids Surf., A*, 2024, **681**, 132804.

11 P. J. Maake, T. P. Mokoena, A. S. Bolokang, N. Hintsho-Mbita, J. Tshilongo, F. R. Cummings, H. C. Swart, E. I. Iwuoha and D. E. Motaung, *Mater. Adv.*, 2022, **3**, 7302–7318.

12 S. Singh and S. Sharma, *Sens. Actuators, B*, 2022, **350**, 130798.

13 P. V. Kamat, *J. Phys. Chem. C*, 2012, **116**, 11849–11851.

14 A. N. Enyashin and G. Seifert, *Phys. Status Solidi B*, 2005, **242**, 1361–1370.

15 H. Zhang and J. F. Banfield, *J. Mater. Chem.*, 1998, **8**, 2073–2076.

16 T. Gakhar and A. Hazra, *Nanotechnology*, 2021, **32**, 505505.

17 P. Bindra and A. Hazra, *Sens. Actuators, B*, 2019, **290**, 684–690.

18 M. A. Einarsrud and T. Grande, *Chem. Soc. Rev.*, 2014, **43**, 2187–2199.

19 T. Gakhar and A. Hazra, *Nanoscale*, 2020, **12**, 9082–9093.

20 M. M. Arafat, A. S. M. A. Haseeb and S. A. Akbar, *Sensors*, 2014, **14**, 13613–13627.

21 J. S. Kim, H. W. Yoo, H. O. Choi and H. T. Jung, *Nano Lett.*, 2014, **14**, 5941–5947.

22 K. Lee, R. Gatensby, N. McEvoy, T. Hallam and G. S. Duesberg, *Adv. Mater.*, 2013, **25**, 6699–6702.

23 S. Anantharaj, S. Kundu and S. Noda, *J. Mater. Chem. A*, 2020, **8**, 4174–4192.

24 J. Huang, Y. Jiang, T. An and M. Cao, *J. Mater. Chem. A*, 2020, **8**, 25465–25498.

25 W. Y. Lee, K. Kim, S. H. Lee, J. H. Bae, I. M. Kang, M. Park, K. Kim and J. Jang, *ACS Omega*, 2022, **7**, 10262–10267.

26 X. Chen, X. Chen, Y. Han, C. Su, M. Zeng, N. Hu, Y. Su, Z. Zhou, H. Wei and Z. Yang, *Nanotechnology*, 2019, **30**, 445503.

27 W. Zhao, R. Yan, H. Li, K. Ding, Y. Chen and D. Xu, *Mater. Lett.*, 2023, **330**, 133386.

28 N. Yue, J. Weicheng, W. Rongguo, D. Guomin and H. Yifan, *J. Mater. Chem. A*, 2016, **4**, 8198–8203.

29 J. H. Kim, A. Mirzaei, H. W. Kim and S. S. Kim, *Sens. Actuators, B*, 2020, **313**, 128040.

30 J. H. Kim, A. Mirzaei, H. W. Kim and S. S. Kim, *Sens. Actuators, B*, 2019, **296**, 126659.

31 Y. Sun, B. Wang, S. Liu, Z. Zhao, W. Zhang, W. Zhang, K. Suematsu and J. Hu, *Sens. Actuators, B*, 2023, **380**, 133341.

32 S. Y. Choi, Y. Kim, H. S. Chung, A. R. Kim, J. D. Kwon, J. Park, Y. L. Kim, S. H. Kwon, M. G. Hahm and B. Cho, *ACS Appl. Mater. Interfaces*, 2017, **9**, 3817–3823.

33 W. Y. Chen, X. Jiang, S. N. Lai, D. Peroulis and L. Stanciu, *Nat. Commun.*, 2020, **11**, 1–10.

34 C. Zhao, X. Gan, Q. Yuan, S. Hu, L. Fang and J. Zhao, *Adv. Opt. Mater.*, 2018, **6**, 1–7.

35 P. Dwivedi, S. Das and S. Dhanekar, *ACS Appl. Mater. Interfaces*, 2017, **9**, 21017–21024.

36 M. Barzegar, M. Berahman and A. I. Zad, *Beilstein J. Nanotechnol.*, 2018, **9**, 608–615.

37 J. W. Yoon and J. H. Lee, *Lab Chip*, 2017, **17**, 3537–3557.

38 R. Bhardwaj, V. Selamneni, U. N. Thakur, P. Sahatiya and A. Hazra, *New J. Chem.*, 2020, **44**, 16613–16625.

39 R. Bhardwaj and A. Hazra, *ACS Appl. Nano Mater.*, 2022, **5**, 15507–15517.

40 R. Bhardwaj, U. N. Thakur, P. Ajmera, R. Singhal, Y. Rosenwaks and A. Hazra, *ChemNanoMat*, 2022, **8**, e202100448.

41 S. J. Panchu, K. Raju, H. C. Swart, B. Chokkalingam, M. Maaza, M. Henini and M. K. Moodley, *ACS Omega*, 2021, **6**, 4542–4550.

42 R. Abinaya, J. Archana, S. Harish, M. Navaneethan, S. Ponnusamy, C. Muthamizhchelvan, M. Shimomura and Y. Hayakawa, *RSC Adv.*, 2018, **8**, 26664–26675.

43 A. M. Van Der Zande, P. Y. Huang, D. A. Chenet, T. C. Berkelbach, Y. You, G. H. Lee, T. F. Heinz, D. R. Reichman, D. A. Muller and J. C. Hone, *Nat. Mater.*, 2013, **12**, 554–561.

44 V. Fominski, M. Demin, V. Nevolin, D. Fominski, R. Romanov, M. Gritskevich and N. Smirnov, *Nanomaterials*, 2020, **10**, 653.

45 Z. Liu, H. Lv, Y. Xie, J. Wang, J. Fan, B. Sun, L. Jiang, Y. Zhang, R. Wang and K. Shi, *J. Mater. Chem. A*, 2021, **10**, 11980–11989.

46 J. Guo, Y. Li, B. Jiang, H. Gao, T. Wang, P. Sun, F. Liu, X. Yan, X. Liang, Y. Gao, J. Zhao and G. Lu, *Sens. Actuators, B*, 2020, **310**, 127780.

47 G. Yang, C. Cao, H. Zhong, Y. Cheng, W. Zhang and D. Wang, *Colloids Surf., A*, 2023, **659**, 130813.